International Journal of Nanomedicine

Dovepress
open access to scientific and medical research

Open Access Full Text Article

ORIGINAL RESEARCH

In vitro/In vivo Evaluations of Hydroxyapatite Nanoparticles with Different Geometry

Weitang Sun[1], Jingbin Zhong[1], Buyun Gao[2], Jieling Feng[1], Zijie Ye[1], Yueling Lin[3], Kelan Zhang[3], Wenqi Su[3], Shibo Zhu[1], Yinghua Li[4], Wei Jia[1]

[1]Department of Pediatric Urology, Guangzhou Women and Children's Medical Center, Guangzhou Medical University, Guangzhou, People's Republic of China; [2]School of Pharmacy, Fudan University, Shanghai, People's Republic of China; [3]Institute of Pediatrics, Guangzhou Women and Children's Medical Center, Guangzhou Medical University, Guangzhou, People's Republic of China; [4]Center Laboratory, Guangzhou Women and Children's Medical Center, Guangzhou Medical University, Guangzhou, People's Republic of China

Correspondence: Wei Jia, Email jiawei198044@hotmail.com

International Journal of Nanomedicine downloaded from https://www.dovepress.com/
For personal use only.

Purpose: Hydroxyapatite-based nanoparticles have found diverse applications in drug delivery, gene carriers, diagnostics, bioimaging and tissue engineering, owing to their ability to easily enter the bloodstream and target specific sites. However, there is limited understanding of the potential adverse effects and molecular mechanisms of these nanoparticles with varying geometries upon their entry into the bloodstream. Here, we used two commercially available hydroxyapatite nanoparticles (HANPs) with different geometries (less than 100 nm in size each) to investigate this issue.

Methods: First, the particle size, Zeta potential, and surface morphology of nano-hydroxyapatite were characterized. Subsequently, the effects of 2~2000 μM nano-hydroxyapatite on the proliferation, migration, cell cycle distribution, and apoptosis levels of umbilical vein endothelial cells were evaluated. Additionally, the impact of nanoparticles of various shapes on the differential expression of genes was investigated using transcriptome sequencing. Additionally, we investigated the in vivo biocompatibility of HANPs through gavage administration of nanohydroxyapatite in mice.

Results: Our results demonstrate that while rod-shaped HANPs promote proliferation in Human Umbilical Vein Endothelial Cell (HUVEC) monolayers at 200 μM, sphere-shaped HANPs exhibit significant toxicity to these monolayers at the same concentration, inducing apoptosis/necrosis and S-phase cell cycle arrest through inflammation. Additionally, sphere-shaped HANPs enhance SULT1A3 levels relative to rod-shaped HANPs, facilitating chemical carcinogenesis-DNA adduct signaling pathways in HUVEC monolayers. In vivo experiments have shown that while HANPs can influence the number of blood cells and comprehensive metabolic indicators in blood, they do not exhibit significant toxicity.

Conclusion: In conclusion, this study has demonstrated that the geometry and surface area of HANPs significantly affect VEC survival status and proliferation. These findings hold significant implications for the optimization of biomaterials in cell engineering applications.

Keywords: hydroxyapatite nanoparticle, circulatory system, biocompatibility, survival, proliferation

Introduction

Hydroxyapatite (HA) is a form of calcium phosphate found in human bones and teeth, comprising about 97% of tooth enamel and 65% of bone.[1] Its chemical similarity to these tissues endows synthetic HA with a high affinity for living organisms, thereby rendering it an ideal material for biomedical applications.[2,3] Owing to advancements in nanotechnology, nano-structured HA has attracted significant attention in various biomedical fields, including diagnosis, medical treatment and tissue engineering.[4–20] Unlike other potential nanoparticles, hydroxyapatite nanoparticles (HANPs) possess a large surface area and contain numerous -OH groups and Ca^{2+} cations, which can effectively adsorb therapeutic agents (TAs) and target ligands featuring acidic groups such as carboxyl (-COO-) and phosphate groups. As nanocarriers, the unique surface properties and pH-responsive solubility of HANPs facilitate their functionalization and design for targeted delivery of pH-responsive Tas.[4,17,19] For example, the development of the use of HANPs for vaccine adjuvant is evolving

Received: 24 May 2024
Accepted: 30 July 2024
Published: 23 August 2024

© 2024 Sun et al. This work is published and licensed by Dove Medical Press Limited. The full terms of this license are available at https://www.dovepress.com/terms.php and incorporate the Creative Commons Attribution – Non Commercial (unported, v3.0) License (http://creativecommons.org/licenses/by-nc/3.0/). By accessing the work you hereby accept the Terms. Non-commercial uses of the work are permitted without any further permission from Dove Medical Press Limited, provided the work is properly attributed. For permission for commercial use of this work, please see paragraphs 4.2 and 5 of our Terms (https://www.dovepress.com/terms.php).

well.[21–25] Additionally, HANPs may be combined with contrast agents for molecular imaging in diagnostics, or integrated with organic molecules to develop porous scaffolds for tissue engineering.[5,7–9,11–15,18,19,26] However, the effects of these HANPs on organisms are not yet fully understood, posing a significant obstacle to their application.

Epidemiological studies indicate that exposure to nanoparticles may exacerbate cardiovascular disease and potentially disrupt cardiovascular homeostasis in healthy individuals.[27–29] The underlying mechanisms behind these cardiovascular effects remain not well understood. The leading hypothesis proposes that nanoparticles may induce vascular inflammation and systemic release of cytokines, potentially impacting cardiovascular endpoints. In practical applications, these nanoparticles have the potential to enter the cardiovascular system through ingestion (gastrointestinal), inhalation (respiratory), injection (blood circulation), or implant fragments.[8,29–32] As vascular endothelial cells (VECs) constitute a protective barrier between blood and tissues, the direct contact between nanoparticles and VECs holds pathogenic relevance.[28] Animal studies have demonstrated that biomolecular delivery agents based on HANPs can readily cross the blood-brain barrier after injection, indicating these nanoparticles could inevitably have potential effects on VECs.[8,16,17,30] Therefore, investigating the interaction between HANPs and VECs is critical before endorsing their widespread and safe use. Previous reports suggest that HANPs may inhibit nitric oxide (NO) synthesis and adversely affect the viability and function of normal human umbilical vein endothelial cells (HUVECs).[33] Similarly, HANPs demonstrate concentration-dependent toxicity on both normal HUVECs and microvascular endothelial cells, highlighting potential limitations in their application due to cardiovascular effects.[9,34,35]

It has been demonstrated that the flow, edge, and adhesion properties of nanoparticle-based biomolecular delivery agents in the vasculature depend on their size and geometry.[36] A noteworthy study in human vascular smooth muscle cells (VSMCs) revealed that small, phagocytosable HANPs elicit a stronger inflammatory response and greater cell death-inducing capability than larger HA particles.[37] Additionally, studies indicate that tiny HANPs can induce pro-inflammatory effects in human monocytes/macrophages relative to larger HA particles.[38,39] These findings suggest that the size of HANPs is closely linked to adverse cardiovascular effects, playing a potential causal role. HANPs are engineered in various geometries, including rods, spheres, needles, and sheets, tailored to specific medical applications.[4,6,7,10,15] However, the impact of HANPs geometry on cardiovascular function remains unclear. As VEC damage and dysfunction constitute common pathological features of several cardiovascular diseases, our experiment sought to determine whether HANPs geometry affects the survival and proliferation of VECs and to elucidate the underlying molecular mechanisms. To date, research in this area has been limited. The primary goal of our study is to advance understanding of the effects of HANPs exposure in the bloodstream, with a focus on the impact of HANPs geometry.

Materials and Methods

Preparation of HANPs Culture Media with Various Concentrations

Commercially available rod-shaped HANPs (677418, Sigma, Missouri, USA) and sphere-shaped HANPs (900194, Sigma) were accurately weighed and designated as rods and spheres, respectively. The HANPs suspensions were prepared at a concentration of 20 mM in a 2 mL standard flask containing 1 mL of 70% ethanol (anhydrous ethanol, HB15-AR, Guangzhou chemical reagent factory, Guangzhou, China) and were sterilized for 30 min. Following this, the suspension was centrifuged at 5000 rpm for 10 min to eliminate the ethanol. Subsequently, the suspension was washed thoroughly with sterile saline (ZH13180052, RockTech, Guangzhou, China) and once again centrifuged at 5000 rpm for 10 min to eliminate the saline. The rods or spheres HANPs with various concentrations were dissolved in sterile saline or ECM culture medium (1001, ScienCell, California, USA). The resulting samples were stored at 4°C for subsequent biological studies.

Characterization

The morphology and selected area electron diffraction (SAED) pattern of HANPs were observed using a Hitachi (Tokyo, Japan) 8100 transmission electron microscope (TEM). The size distribution of rods or spheres HANPs was determined by analyzing TEM images with ITEM software, allowing for precise measurements.[40] X-ray diffraction (XRD)

measurements were performed using a Bruker D8 Advance diffractometer (Karlsruhe, Germany) equipped with Cu Kα radiation (λ=0.15418nm). The XRD measurements were carried out at a voltage of 40 kV and a current of 40 mA, with a scanning rate of 1°/s and a scanning range of 5°-80°. For the identification of chemical element composition, X-ray photoelectron spectroscopy (XPS) was carried out using a Thermo Fisher Scientific (USA) Escalab 250Xi spectrometer with Al Kα radiation for excitation.[41] Fourier Transform infrared spectra (FTIR) were obtained using a Bruker Tensor 27 spectrometer (Karlsruhe, Germany), covering a range of 200–4000 cm^{-1}. Raman spectra were acquired using a Horiba LabRAM HR Evolution laser Raman spectrometer (Paris, France), employing He laser beam excitation within the 200–3000 cm^{-1} range. The specific surface area was evaluated through N2 adsorption utilizing a fully automatic surface area system, the Micromeritics ASAP 2020 plus HD88 from the United States. Before measurements, the samples were subjected to outgassing at 120 °C for 120 min. Finally, these rods or spheres HANPs, which were dissolved in sterile saline or ECM culture medium, were transferred into the cuvette for zeta potential measurement using a Malvern Zetasizer Nano ZSE instrument (Malvern, UK) and their hydrodynamic size and polydispersity (PDI) determined by the Zetasizer Nano ZS90.

Human Umbilical Vein Vascular Endothelial Cells (HUVEC) Isolation, Culture, and Identification

To isolate HUVECs, a fresh umbilical cord is obtained from the delivery of a healthy woman. The ethical approval for the use of human umbilical cords has been granted by the Ethics Committee of the Guangzhou Medical University affiliated Women and Children's Medical Center, under approval number 2017103104. All umbilical cords utilized in the experiment were obtained with written informed consent from the donors, adhering to the principles outlined in the Declaration of Helsinki. The procedure involves the following steps: Inserting a 50 mL syringe filled with 1×PBS into the umbilical vein. Repeatedly flush the umbilical vein with PBS until all blood clots are expelled. Injecting 40 mL of 0.25% trypsin-EDTA solution (T1350, Solarbio, Beijing, China) into the umbilical vein allows the digestion to proceed for 15 minutes. Stopping the trypsin digestion occurs by slowly flushing the umbilical vein with fetal bovine serum (FBS-S500, NEWZERUM, Christchurch, New Zealand). The cells released during digestion are then collected and resuspended in an ECM medium. Seeding the resuspended cells in 6-well plates and incubating them at 37 °C in a 5% CO2 humidified atmosphere follows. Changing the medium occurs every 2 days. The cells reach 90% confluency, typically achieved by passage 0 (P0). Identifying HUVECs is done using an endothelial cell marker, such as an anti-mouse CD31 monoclonal antibody (GB12064, Servicebio, Wuhan, China) or anti-rabbit Von Willebrand Factor (VWF) polyclonal antibody (GB11020, Servicebio). Seeding HUVECs at passage 1 (P1) in 6-well plates with 1000,00 cells per well and incubating them for 8 days facilitates observation of the cell growth curve. Cells in the logarithmic growth phase at passage 2 (P2) are seeded in new 6-well plates with 1000,00 cells per well and incubated for 4 days to obtain a HUVEC monolayer with a cell layer fusion of 90%.[42]

Immunofluorescence Staining and Quantifications

The localization of proteins in cultured cells was assessed using the following protocol. Firstly, the cells were fixed with 4% paraformaldehyde for 20 min at room temperature. Subsequently, the cells were permeabilized with 0.5% Triton X-100 (GRNF103-CHMP304003, Servicebio) in PBS for 15 minutes. To prevent non-specific binding, the cells were blocked with a PBS solution containing 1% bovine serum albumin (BSA) for 1 hour. Following this, the cells were incubated overnight at 4 °C with specific primary antibodies, including rabbit anti-Ki67 polyclonal antibody (GB111499, Servicebio), mouse anti-CD31 monoclonal antibody, and rabbit anti-VWF polyclonal antibody, in accordance with the manufacturer's instructions. After three PBS washes, the cells were incubated with fluorescently labeled secondary antibodies, including Cy3-labeled donkey anti-rabbit immunoglobulin G (IgG, GB21403, Servicebio) and fluorescein isothiocyanate (FITC)-labeled goat anti-mouse IgG (GB22301, Servicebio). Additionally, the actin cytoskeleton was stained using FITC-conjugated phalloidin (G1028, Servicebio). Nuclei were counterstained with Hoechst 33258 (G1011, Servicebio). Images were captured using a Leica TCS SP5 confocal laser scanning microscope (Wetzlar, Germany) at

20× magnification. To quantify the fluorescence intensity of Ki67, CD31, and VWF, five independent microscopic fields were subjected to analysis using ImageJ software (Bethesda, ML, USA).

In vitro Toxicity and Live/Dead Cell Staining Study

To assess the cytotoxicity of rods and spheres HANPs, evaluations were conducted on HUVEC monolayers. The rods and spheres HANPs were dissolved in ECM medium, while ECM medium alone acted as a blank control. Initially, HUVECs were cultured in 96-well plates with a seeding density of 3500 cells per well and were allowed to form a monolayer over a period of 4 days. Subsequently, the HUVEC monolayers were exposed to various concentrations of rod and sphere-shaped HANPs in ECM medium for 24 hours. Cell viability was assessed using a microplate reader (Multiskan GO, Thermo Fisher, Karlsruhe, Germany) by measuring the absorbance at 450 nm after adding 10 μL of Cell Counting Kit-8 (CK04, Dojindo, Shanghai, China) to each well and incubating them for 4 hours. The experiment was conducted with three biological replicates.

To further analyze the viability of HUVEC monolayers exposed to rods or spheres HANPs, a live/dead cell staining assay was conducted using a calcein AM (for live cells, green fluorescence) and propidium iodide (PI, for dead cells, red fluorescence) assay kit (L3224, InvitrogenTM, Shanghai, China), in accordance with a previously established protocol. This staining facilitated the differentiation between live and dead cells and was utilized to evaluate the impact of rod and sphere-shaped HANPs on cell viability, in comparison with the control group.[43,44]

Apoptosis and Cell Cycle Analyses

After exposing HUVEC monolayers to rods or spheres HANPs ECM medium with varying concentrations, or to ECM medium alone for 24 hours, the monolayers were washed three times with 1× PBS. Subsequently, the monolayers were treated with 0.25% trypsin to obtain single-cell suspensions. The suspension was then centrifuged at 1000 rpm for 5 minutes, the supernatant discarded, and the cells washed once with 1× PBS. The cells were stained with the Annexin V-647 and PI kit (KGAV115, KeyGEN, Jiangsu, China) for 15 minutes, protected from light, and analyzed using flow cytometry (DB FACSCanto, Franklin Lakes, NJ, USA) to assess apoptosis.

HUVEC monolayers were treated as previously described to obtain single-cell suspensions for cell cycle analysis. The suspension was centrifuged at 1000 rpm for 5 minutes, the supernatant discarded, and the cells were washed once with pre-chilled 1× PBS. The cells were then resuspended in pre-chilled 70% ethanol and stored at 4°C for 12 hours. After centrifugation at 1000 rpm for 5 minutes, the supernatant was discarded, and the cells were stained with a cell cycle kit (SULT1A3052, Beyotime, Jiangsu, China) in a warm bath for 30 minutes, in accordance with the manufacturer's protocol. Cell cycle distribution was subsequently analyzed using DB FACSCanto flow cytometry.

Migration and Wound-Healing Studies

The migration ability of HUVECs was assessed using the transwell assay. Transwell inserts (Corning, 35309) were placed into 24-well plates. The HUVECs were maintained in ECM medium and seeded into the upper chambers with 10,000 cells per chamber. They were incubated for 2 days to obtain a HUVEC monolayer. Then, rods and spheres HANPs ECM medium at a concentration of 200 μM or ECM medium alone were added to the underlying wells and further incubated for 24 hours respectively. The migrated cells were fixed with 4% paraformaldehyde (Aladdin, SULT1A304190, Shanghai, China), subsequently washed with PBS, and then stained with crystal violet. The transwell inserts were visualized using an inverted fluorescence microscope (Leica, DMi8, Wetzlar, Germany), and cell migration quantification occurred in five independent microscope areas using ImageJ software.

The wound-healing ability was assessed using the scratch assay. The HUVECs were seeded into 6-well plates at a density of 1000,00 cells per well and incubated for 4 days to achieve a HUVEC monolayer. Horizontal lines were drawn using micropipette tips in each well to simulate wounds. The HUVEC monolayers were then incubated with rods or spheres HANPs ECM medium at concentrations of 200 μM or with ECM medium alone for 24 hours. The HUVEC monolayers were imaged using an inverted fluorescence microscope equipped with a phase-contrast module. TIFF images of the scratch wound assays were taken at 5× magnification at both 0 and 24 hours. The mean number of cells that migrated back into the wound area was calculated from five individual measurements for each wound, at each time point.

This process was repeated for all biological replicates. The total number of cells in each group was counted to assess wound healing.

Cellular Uptake of HANPs Recorded by TEM

To assess the *c*ellular uptake of rods and spheres HANPs, evaluations were conducted on HUVEC monolayers. HUVECs were cultured in 6-well plates with a seeding density of 100000 cells per well and were allowed to form a monolayer. Then, the HUVEC monolayers were exposed to 200 μM concentrations of rod and sphere-shaped HANPs in ECM medium for 24 hours. After digestion of HUVEC monolayers with 0.25% EDTA trypsin solution and fixation with 2.5% glutaraldehyde protected from light, electron microscopy samples were made according to standard procedures. The uptake of HANPs of these two shapes by HUVEC was observed by TEM.

RNA-Seq and Bioinformatics Analysis

Rods or spheres HANPs at a concentration of 200 μM were dissolved in ECM medium. RNA sequencing was conducted on 9 samples, including 3 control samples treated with ECM medium and 3 samples, each treated with rods or spheres HANPs at a concentration of 200 μM. Total RNA was extracted using Trizol reagent (Invitrogen, 15596018, Massachusetts, USA), and its integrity was assessed by checking the RIN values using an Agilent Bioanalyzer 2100 (Santa Clara, CA, USA). Qualified total RNA was further purified using the RNeasy micro kit and a ribonuclease-free kit. The total RNA was amplified using a low-input rapid amperometry labeling kit, then labeled with a chromogenic label, and hybridized to the Agilent whole human genome microarrays 4 × 44K. The microarrays were scanned using an Agilent microarray scanner. Raw data was normalized using the quantile algorithm and analyzed using Gene Spring software 11.0 (Agilent Technologies). Background signals were calculated, resulting in 27,716 probes appearing at least once. The sequencing was performed at UW Genetics using the BGI platform in Shenzhen, China. The gene expression level was normalized by fragments per kilobase of transcript per million mapped reads (FPKM).

To evaluate the reproducibility between samples, a correlation analysis was conducted using Pearson's correlation coefficient in R for two parallel experiments. Principal component analysis (PCA) was performed using an appropriate R package to uncover the structure and relationships among the samples, which enabled the identification of outliers and the distinction of clusters of samples with high similarity. DESeq2 was used to identify differentially expressed genes (DEGs).

Gene Ontology (GO) is a standardized system for classifying gene functions. It provides a controlled vocabulary and well-defined concepts to comprehensively describe genes and their products. By mapping DEGs to GO terms in the Gene Ontology database, the primary biological functions associated with these genes can be identified. For each GO term, the number of associated genes is calculated, and terms with a false discovery rate (FDR) of ≤ 0.05 are considered significantly enriched. For pathway analysis, the public KEGG (Kyoto Encyclopedia of Genes and Genomes) database was utilized. Metabolic and signal transduction pathways showing significant enrichment among the DEGs were identified through comparison with the genome-wide background. Pathways with an FDR below 0.05 were considered significantly enriched.

To determine if significant differences existed in gene sets for specific terms between the two groups, gene set enrichment analysis (GSEA) was performed using GSEA software (version 4.3.2, Broad Institute, Inc, USA) and the Molecular Signature Database (MSigDB). In this analysis, the gene expression matrix was inputted and genes were ranked using a signal-to-noise normalization method. Enrichment scores and p-values were calculated using the default algorithm, employing 10,000 permutations. A genome size filter was applied to the results, setting a minimum of 15 genes and a maximum of 500 genes for each gene set. Annotated gene sets from the HALLMARK collection version 7.1 were used for enrichment inputs. Gene sets with a normalized enrichment score (NES) greater than 1 and a nominal p-value below 0.05 were deemed significantly enriched.

A network was constructed based on the enrichment analysis of the GO, KEGG, and Reactome databases to capture the relationship between enriched terms, utilizing the Dr. Tom website. Specifically, enrichment terms were defined with criteria including a minimum of 3 overlaps, an enrichment score of at least 1.5, and a p-value below 0.05. Enrichment terms exhibiting a similarity index greater than 0.3 were connected by edges to form a network, facilitating the

visualization of relationships between terms. Additionally, GO enrichment networks specifically pertaining to proliferation and apoptosis-related processes were explored using the Network Analyst online platform. This approach enabled a more focused analysis of the network connections and interactions pertaining to these biological processes.

In vivo Gavage Test and Treatment

The animal experiment was conducted with the approval of the Animal Ethics Committee of Wuhan Servicebio Biotechnology Co., Ltd. (ID: 2022164, Wuhan, China) and adhere to the principles of 3R principles. Balb/c mice at the age of 5 weeks were housed in a controlled environment under specific pathogen-free (SPF) conditions, featuring a 12-hour light-dark cycle, 55±5% humidity, and 25±2°C temperature. Mice had ad libitum access to food and water, with males and females housed separately. Ear tags were placed on the right ear lobes to identify individual mice. Subsequently, the mice were divided into three groups randomly, each containing 12 mice. The experimental group received an oral gavage of rods or spheres HANPs at a dose of 500 μM/kg, whereas the control group received a comparable volume of saline via oral gavage. Electrocardiographic evaluations were conducted on days 1, 7, and 14 after gavage to document the changes in electrical activity associated with the cardiac cycles in each animal. On the 14th day, fresh blood samples were obtained from the tail veins for routine blood tests and to assess serum biochemical parameters related to major organs. Plasma samples were treated with 90% HNO3, evaporated, and then re-dissolved in 1% HNO3. Calcium (Ca) concentrations in the plasma were quantified using inductively coupled plasma mass spectrometry (ICP-MS), employing an Agilent 7700 ICP-MS instrument (Palo Alto, CA, USA). On the 21st day, three animals from each group were randomly selected and euthanized. Major organs were collected, fixed overnight in 4% paraformaldehyde, longitudinally sectioned, embedded in paraffin, and sectioned into 4 μm thick slices using a Leica R^{M2}125RTS paraffin slicer (Wetzlar, Germany). Hematoxylin and Eosin (H&E) staining was performed according to established protocols to examine the histological characteristics of the organs.[45,46]

Statistical Analyses

All data are presented as the mean ± standard deviation (SD), with a minimum sample size of $n \geq 3$. Comparisons among values for groups greater than two were made using a one-way analysis of variance (ANOVA), followed by Tukey's post-hoc test to identify differences between groups. For comparisons involving two groups, a two-tailed, unpaired *t*-test was utilized. Statistical significance was established at p-values less than 0.05. All statistical analyses were conducted using GraphPad Prism 8.0 software.

Results

Characterization of the Commercial HANPs

Figure S1A demonstrates the uniform dispersion of both commercially available rods and spheres HANPs in saline and MEM culture medium. TEM imaging (Figure 1A) reveals that rods HANPs exhibit a high aspect ratio, with length and width ranging from approximately 15–100 nm and 5–30 nm, respectively (Figure 1B). In contrast, spheres HANPs exhibit a more uniform length and width ranging from approximately 15–85 nm. The corresponding SAED patterns (inset in Figure 1A) indicate the polycrystalline nature of rods and spheres HANPs. Wide-angle XRD patterns further confirm the well-crystallized hexagonal structure of rods and spheres HANPs (Figure 1C), with the crystal peaks aligning with the theoretical XRD diffraction peak of HA (No: 09–0432).[6] The XPS spectrum (Figure 1D) reveals the presence of oxygen, calcium, and phosphorus elements in rods and spheres HANPs, consistent with the elemental composition of HA.[6] FTIR spectra (Figure 1E) validate the specific bands of pure phase HA in rods and spheres HANPs, including the hydroxyl stretching at around 3451 cm^{-1} and characteristic absorption bands of $PO4^{3-}$ ions at 1048 cm^{-1}, 962 cm^{-1}, 604 cm^{-1}, and 445 cm^{-1}. Raman spectrum (Figure 1F) confirms the presence of P-O bond vibrations at 1048 cm-1 (ν3), 962 cm^{-1} (ν1), and bending modes of O-P-O bond at 604 cm^{-1} (ν4) and 445 cm^{-1} (ν2). The specific surface areas of rods and spheres HANPs were 32±7 m^2/g and 83±5 m^2/g, respectively (Figure S1B). The surface area of spheres HANPs was approximately 2.5 times larger than that of rods HANPs. The mean zeta potential for rods and spheres HANPs was found to be −1.34 mV and −0.754 mV, respectively (Figure S1C). These findings indicate that rods and spheres HANPs possess

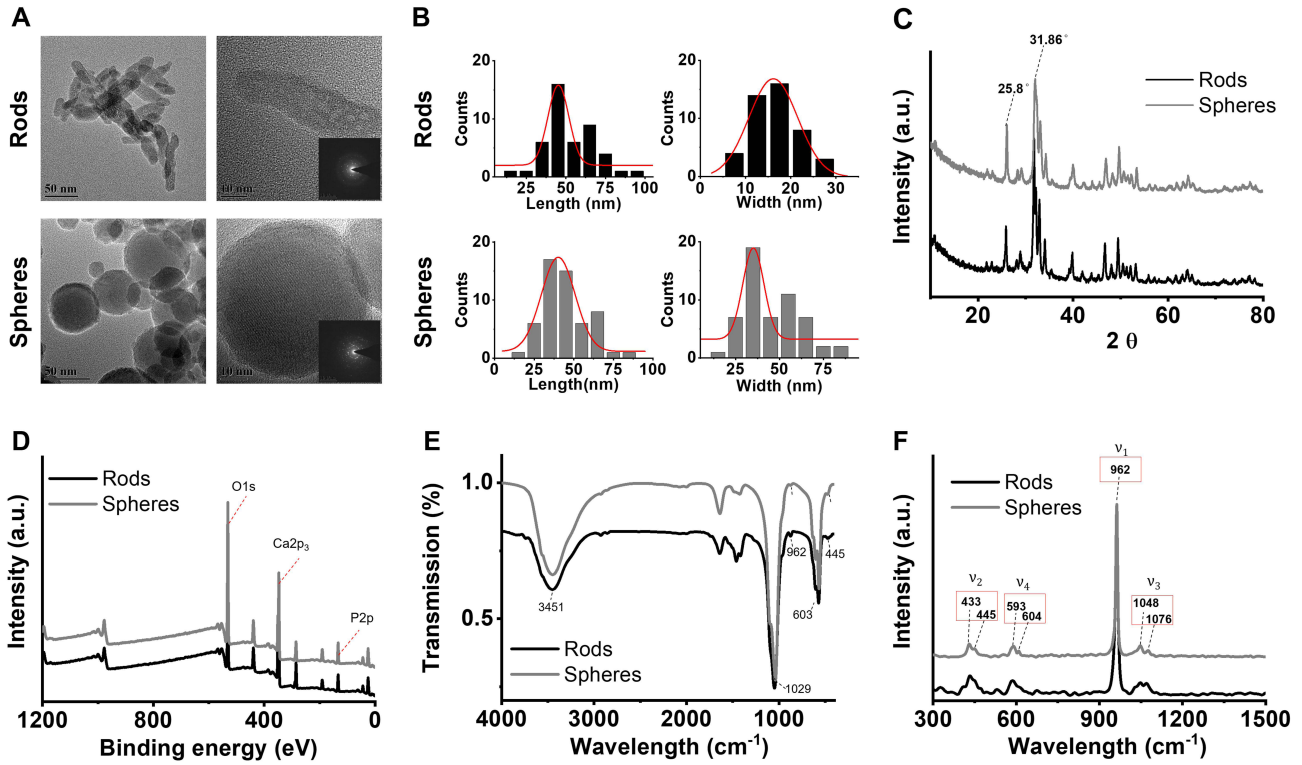

Figure 1 Characterization of rods and spheres HAPNs. (**A**) Representative TEM images of rods and spheres HAPNs with different magnifications; the inset in right panel showed the corresponding SAED pattern of rods and spheres HAPNs. (**B**) The number-average size distribution of rods and spheres HAPNs. (**C**) XRD pattern of rods and spheres HAPNs powder. (**D**) XPS spectra of the rods and spheres HAPNs Figure powder. (**E**) FTIR spectra of the rods and spheres HAPNs powder. (**F**) Raman spectra of freshly prepared rods and spheres HAPNs after storage in ddH2O for 2 days.

similar surface chemistry, though sphere-shaped HANPs have a higher specific surface area and a slightly higher zeta potential compared to rod-shaped HANPs. Moreover, the average hydrodynamic size of rods HANPs was 320.8 nm, 200.1 nm, and 110.6 nm, while the average hydrodynamic size of spheres HANPs was 636.9 nm, 225.2 nm, and 118.3 nm, respectively, at solution pH values of 11, 7.4, and 3 (Figure S2A). However, in ECM cell culture medium, the particle sizes of rod- and sphere-shaped HANPs were found to be very similar (Figure S2B). Moreover, the PDI of the two HANPs was within the range of 0.3–0.6, indicating that the HANPs solution was a relatively stable and uniform dispersion system (Figure S3).

Survival Status of HUVEC Monolayers Correlated with Geometry Following Exposure to HANPs

To establish a vascular endothelial monolayer structure, primary isolated HUVECs were expanded in vitro (Figure S4A), and those in the logarithmic growth stage were selected for subsequent experiments (Figure S4B). The confluence of HUVECs in 96-well culture dishes reached approximately 90% (inset in Figure S4B), signifying the formation of a monolayer structure.[42,43] The cytotoxicity of rods and spheres HANPs was evaluated using a concentration range of 2–2000 μM after 24 hours of exposure, as determined by the CCK-8 assay. The results from Figure 2A demonstrate that the cytotoxicity of rods and spheres HANPs was concentration-dependent. Both types of HANPs showed minimal toxicity at concentrations from 2 to 100 μM, but decreased cell viability was noted at 500 μM for rods HANPs and at 200 μM for spheres HANPs. Notably, the cell viability of HUVEC monolayers exposed to rod-shaped HANPs at 200 μM for 24 hours reached (112±2)%, whereas that of sphere-shaped HANPs at 200 μM for 24 hours was (76±15)%. Considering that concentrations of 100 μM, 200 μM, and 500 μM are commonly used in medical applications involving HANPs-based agents, these concentrations were selected for subsequent cytotoxicity studies. Fluorescent microscopy images of HUVEC monolayers stained with calcein AM (green fluorescence for live cells) and PI (red fluorescence for dead

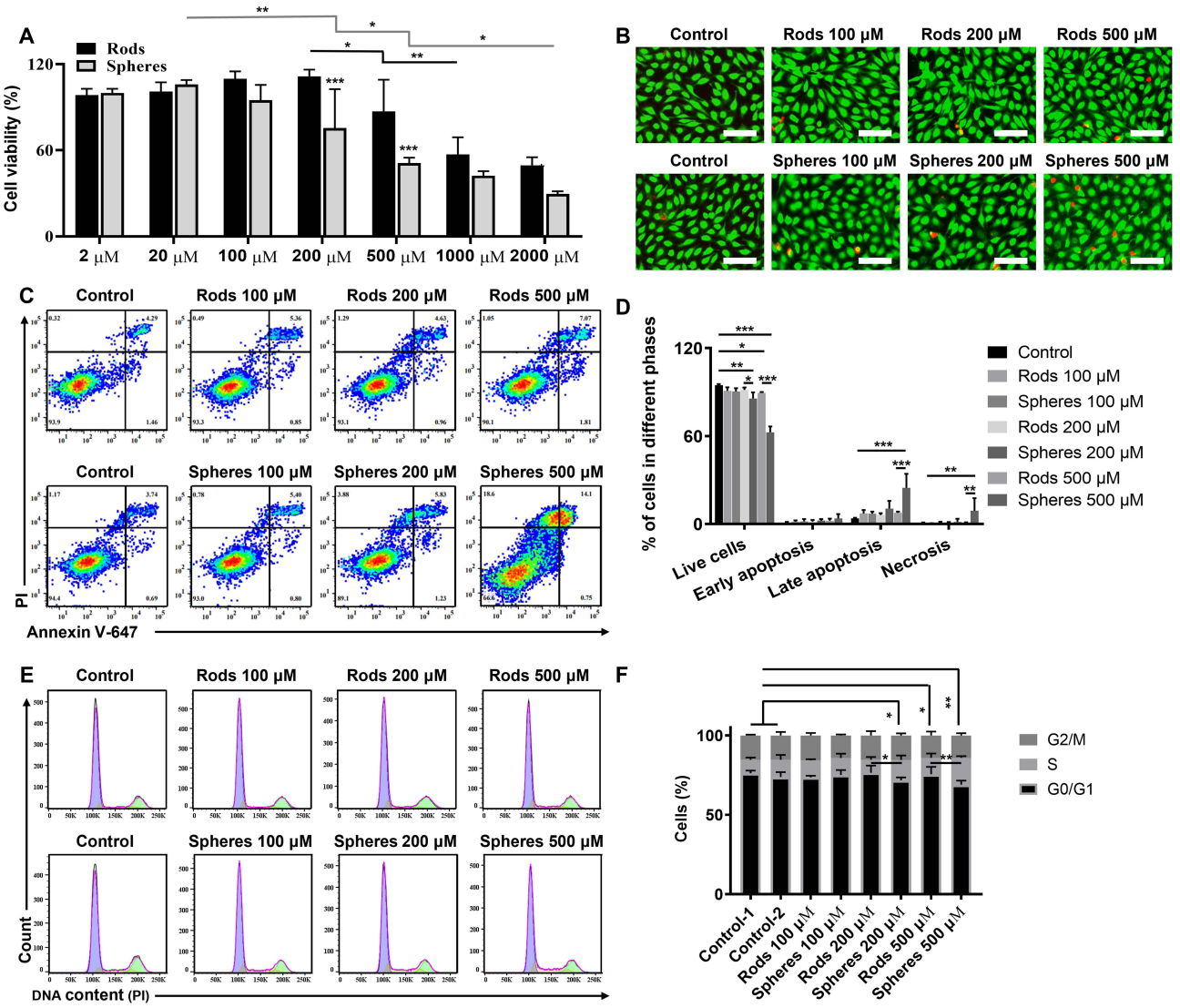

Figure 2 Cytotoxicity and mechanisms of HUVEC monolayer following exposure to rods or spheres HAPNs. (**A**) Cell viability of HUVEC monolayers treated with rods and spheres HAPNs with various concentrations after 24 h. Data are presented as mean ± S.D. (n = 3). (**B**) Representative fluorescence micrographs of HUVEC monolayers stained with calcein AM (live cells, green fluorescence) and PI (dead cells, red fluorescence) after various treatments, scale bars, 20 μm. Experiments were treated three times. (**C**) Representative flow cytometer results of AnnexinV-FITC/PI double-stained cells after various treatments. (**D**) Histogram depicting of the cell population distribution in (**C**). (**E**) Representative cell cycle analysis of cells after various treatments. (**F**) Histogram depicting of the cell population distribution in cell cycle phase in (**E**). Data are presented as mean ± S.D. (n = 3). Statistical differences were calculated via one-way ANOV A with a Tukey post-hoc test for multiple comparisons. *p < 0.05, **p < 0.01, ***p < 0.001.

cells) after treatment with rods or spheres HANPs provided similar results (Figure 2B). The results also showed that high concentrations of HANPs led to an increase in dead cells, and at the same concentration, HUVEC monolayers exposed to sphere-shaped HANPs resulted in more dead cells.

To investigate the mechanism of toxicity, cell apoptosis was assessed using Annexin V-FITC/PI double-staining. Figure 2C demonstrates that rods and spheres HANPs induced minimal late apoptosis in the HUVEC monolayer at a concentration of 100 μM after 24 hours of exposure, indicating minimal toxicity at this concentration, independent of their geometry. At 200 μM, flow cytometry analysis detected that spheres HANPs triggered more early apoptosis, late apoptosis, and necrosis in the HUVEC monolayers compared to rods HANPs. When the concentration was increased to 500 μM, rods HANPs mainly induced late apoptosis, while spheres HANPs caused more late apoptosis/necrosis (Figure 2C and D). Cell cycle distribution analysis was conducted to assess nuclear DNA damage resulting from HANPs exposure. The cell cycle of the HUVEC monolayer remained unaffected by exposure to rods HANPs at 200

μM; however, it was primarily arrested at the S-phase following exposure to spheres HANPs at the same concentration (Figure 2E and F), implying a suppression of DNA replication.

Proliferation Analysis of HUVEC Monolayers Following Exposure to HANPs with Different Geometry

To further explore the impact of rods or spheres HANPs on the nucleus, Ki67 immunofluorescence staining, a mitotic marker, was performed. The results showed that rods HANPs did not affect cell proliferation in the HUVEC monolayer at 200 μM, whereas spheres HANPs at 200 μM significantly inhibited cell proliferation (Figure 3A and B). At a higher concentration of 500 μM, both rods and spheres HANPs significantly inhibited nucleus proliferation in the HUVEC monolayer, indicating a geometry-dependent effect (Figure 3A and B). Interestingly, when HANPs were present in the lower layers of transwell chambers, they markedly promoted the migration of HUVECs from the upper to the lower layers, an effect that intensified at a concentration of 500 μM (Figure 3C and D). Considering the repair capabilities of the vascular endothelium, the study investigated how HANPs' geometry post-exposure influences the HUVEC monolayers' repair function following a scratch injury and 24-hour exposure to rods or spheres HANPs. Compared to controls, at 200 μM, rods HANPs promoted the "scratches" healing efficiency, while spheres HANPs did not affect the healing efficiency of "scratches" ($p>0.05$), at 500 μM, rods HANPs did not affect the healing efficiency of "scratches" ($p>0.05$).

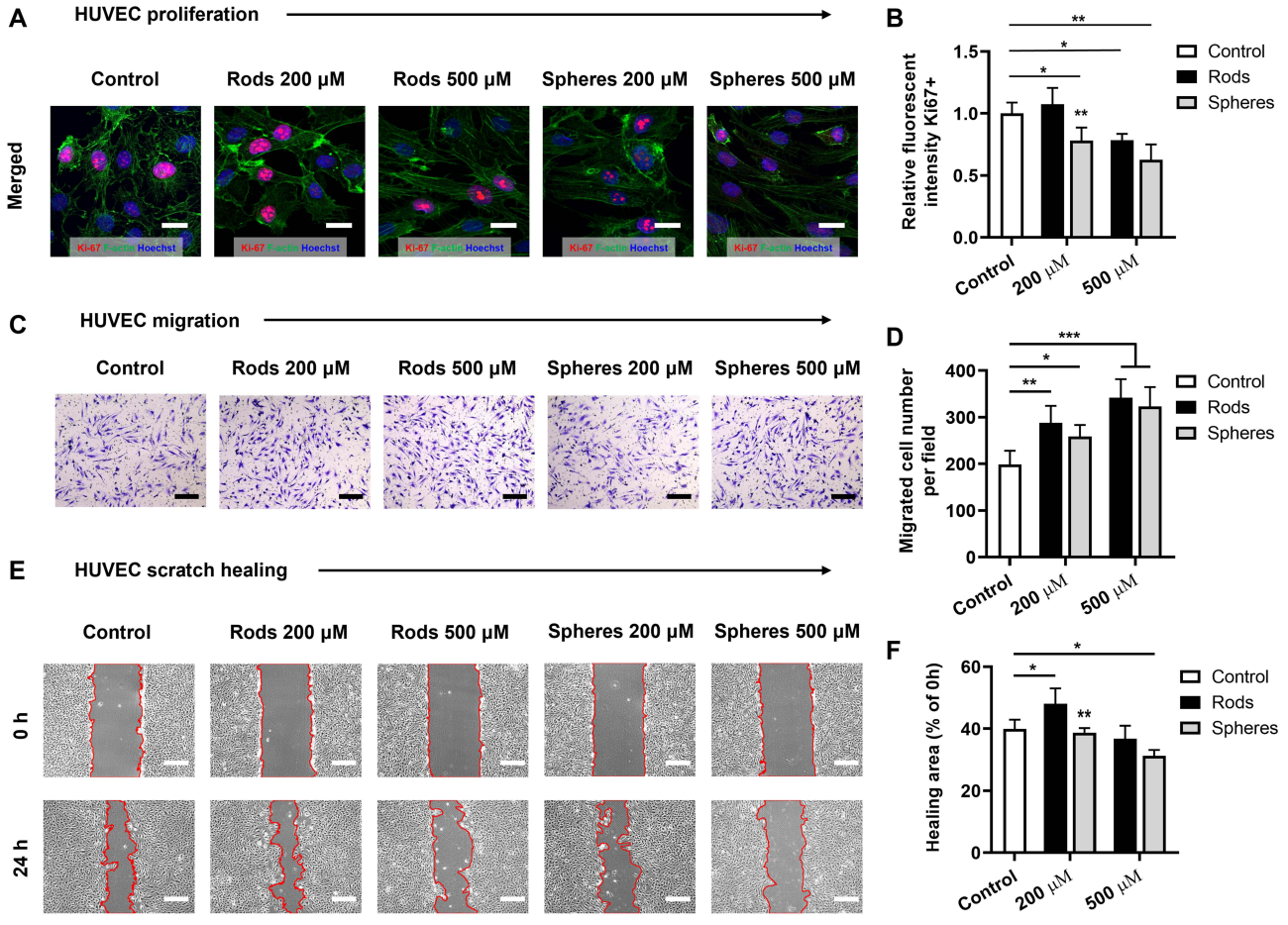

Figure 3 Proliferative function of HUVEC monolayers after exposure to rods or spheres HAPNs. A, B, Representative immunostaining of Ki67+ (**A**) and relative quantification of Ki67+ (**B**) in HUVEC monolayers after various treatments. (**C** and **D**) Representative transwell analysis images (**C**) and relative quantification of migrated HUVECs from HUVEC monolayer (**D**) after various treatments. E, F, Representative micrographs of HUVEC monolayer scratch at 0 h (upper panels) and 24 h (lower panels) (**E**) and relative quantification of cells (**F**) that migrated back into the wound after various treatments. Scale bar, (**A**) 20 μm; (**C**) 200 μm; (**E**) 400 μm. Data are presented as mean ± S.D. (n = 3). Statistical differences were calculated via one-way ANOVA with a Tukey post-hoc test for multiple comparisons. *p < 0.05, **p < 0.01, ***p < 0.001.

In contrast, spheres HANPs affected the healing efficiency of "scratches" ($p<0.05$). This suggests that higher doses of spheres HANPs exposure impair the "scratches" repair function of HUVEC monolayers (Figure 3E and F).

Transcriptomic Analysis

The varied survival status of HUVEC monolayers after exposure to HANPs of different geometries prompted an investigation into the underlying mechanisms. To address this issue, high-throughput RNA sequencing (RNA-seq) analysis was conducted. A 24-hour exposure to 200 μM rods or spheres HANPs was chosen for this assay because this concentration maintained cell viability above 75%. HUVEC monolayers were incubated in 12-well plates, with ECM alone (control), rod-shaped HANPs, and sphere-shaped HANPs at 200 μM each added separately and incubated for 24 hours. RNA from each group was collected and subjected to RNA-seq for transcriptomic analysis.

To assess differences between groups, Pearson correlation coefficient analysis was utilized to compare gene distances using normalized fragment counts. In Figure 4A, samples exhibited close correlation, with minimum Pearson's coefficients of 0.997 within groups and 0.993 between samples from different groups, highlighting the sequencing data's high quality and reliability. Principal component analysis (PCA) was performed to assess the aggregation of cell samples. PCA, a dimensionality reduction technique, simplifies high-dimensional data complexity and aids in identifying key features. Figure 4B projects the samples onto a two-dimensional plane using the first and second principal components (PSULT1A3 and PRNF103-CHMP3). Significant differences were observed between the three groups. PSULT1A3 and PRNF103-CHMP3 contributed 75.77% and 10.07% to the variation, respectively. The control group exhibited a negative distribution along the PRNF103-CHMP3 axis, whereas the rods and spheres HANPs groups predominantly showed positive distribution. Furthermore, PSULT1A3 effectively distinguished the three groups, indicating unique gene expression patterns and cellular responses to the varying HANPs geometries.

The RNA differential expression analysis identified 5 DEGs between the rods HANPs group and the control group, comprising 1 up-regulated DEG and 4 down-regulated DEGs. Between the spheres HANPs group and the control group, 3 DEGs were identified, comprising 2 up-regulated DEGs and 1 down-regulated DEG. Additionally, 1 up-regulated DEG was identified between the rods and spheres HANPs groups (Figure S5A). Significant DEGs were determined based on fold change and significance (q-value), with their distribution illustrated in the volcano plot (Figure 4C). In the HUVEC monolayer treated with rod-shaped HANPs culture solution, POSTN was identified as the significantly up-regulated gene compared to the control.

In contrast, the significantly down-regulated genes included SULT1A3, RNF103-CHMP3, SFTPB, and COL1A1. For the HUVEC monolayer treated with spheres HANPs culture solution, POSTN and CCL2 were significantly up-regulated, while SFTPB was significantly down-regulated. Compared to the rods HANPs group, SULT1A3 was the most significantly up-regulated gene in the HUVEC monolayer exposed to spheres HANPs. Differentially expressed genes were further visualized in expression heat maps (Figure 4D), highlighting distinct gene expression patterns among the three groups. The gene correlation heat map (Figure 4E) revealed significant correlations among the expression values of down-regulated genes SULT1A3, RNF103-CHMP3, SFTPB, and COL1A1, as well as among the up-regulated genes POSTN and CCL2. Comparing the distribution of expression levels of significant DEGs in HUVEC monolayers treated with rods and spheres HANPs culture medium against the control group further confirmed the differences in gene expression patterns between groups (Figure S5B).

The analysis of DEGs revealed several signaling molecules of particular interest due to their central roles in determining cell fate. Compared to the control group, reduced expression of SULT1A3, RNF103-CHMP3, and COL1A1 in HUVEC monolayers treated with rods HANPs was associated with restricted biological processes, including cellular responses to fluoride and vitamin E, tooth mineralization, regulation of exosomal secretion, and the NMDA selective glutamate receptor signaling pathway (Figure 5A). Conversely, elevated expression of CCL2 in HUVEC monolayers treated with spheres HANPs was linked to the promotion of biological processes such as helper T cell extravasation, cellular response to vitamin K, negative regulation of natural killer cell chemotaxis, and the negative regulation of vascular endothelial cell proliferation, as well as bone regeneration. When comparing spheres HANPs-treated HUVEC monolayers with rods HANPs-treated HUVEC monolayers, elevated expression of SULT1A3 in the spheres HANPs group was found to promote biological processes, including the NMDA selective glutamate receptor signaling pathway, calcineurin-mediated signaling, dopamine catabolic process, flavonoid metabolic process, and catecholamine metabolic process. The KEGG pathway and network analyses revealed that several signaling pathways were

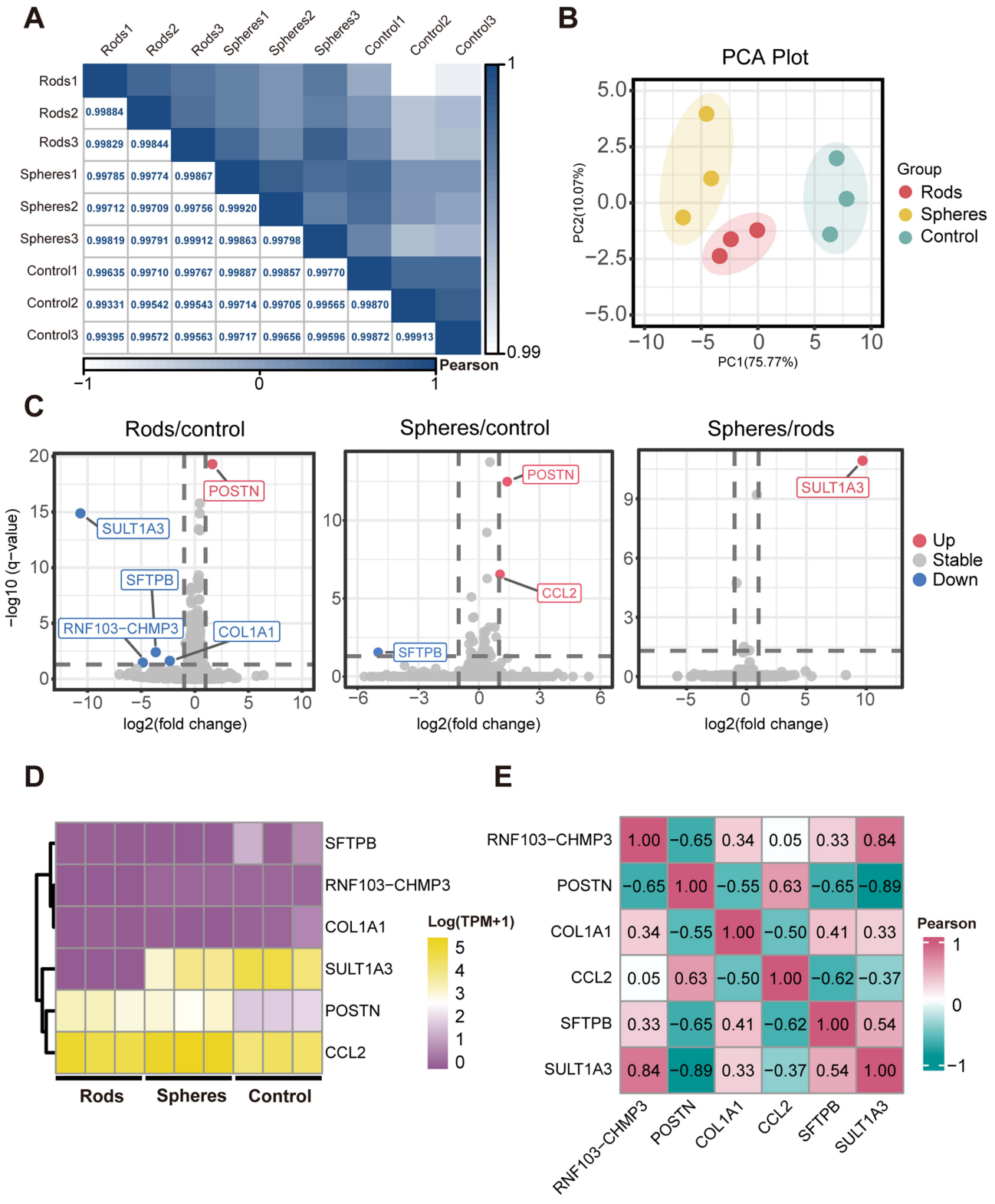

Figure 4 Gene expression pattern of HUVEC monolayer following exposure to rods or spheres HAPNs. (**A**) Correlation heat map of the tested samples. (**B**) PCA analysis of the tested samples. (**C**) Volcano plot of the DECs after two groups comparison. (**D**) Heat map of DECs of the tested samples. (**E**) Correlation heat map of DEGs.

significantly downregulated in HUVEC monolayers treated with rods HANPs compared to the control group, including pathways related to chemical carcinogenesis-DNA adducts, ECM-receptor interaction, platelet activation, necroptosis, and endocytosis.

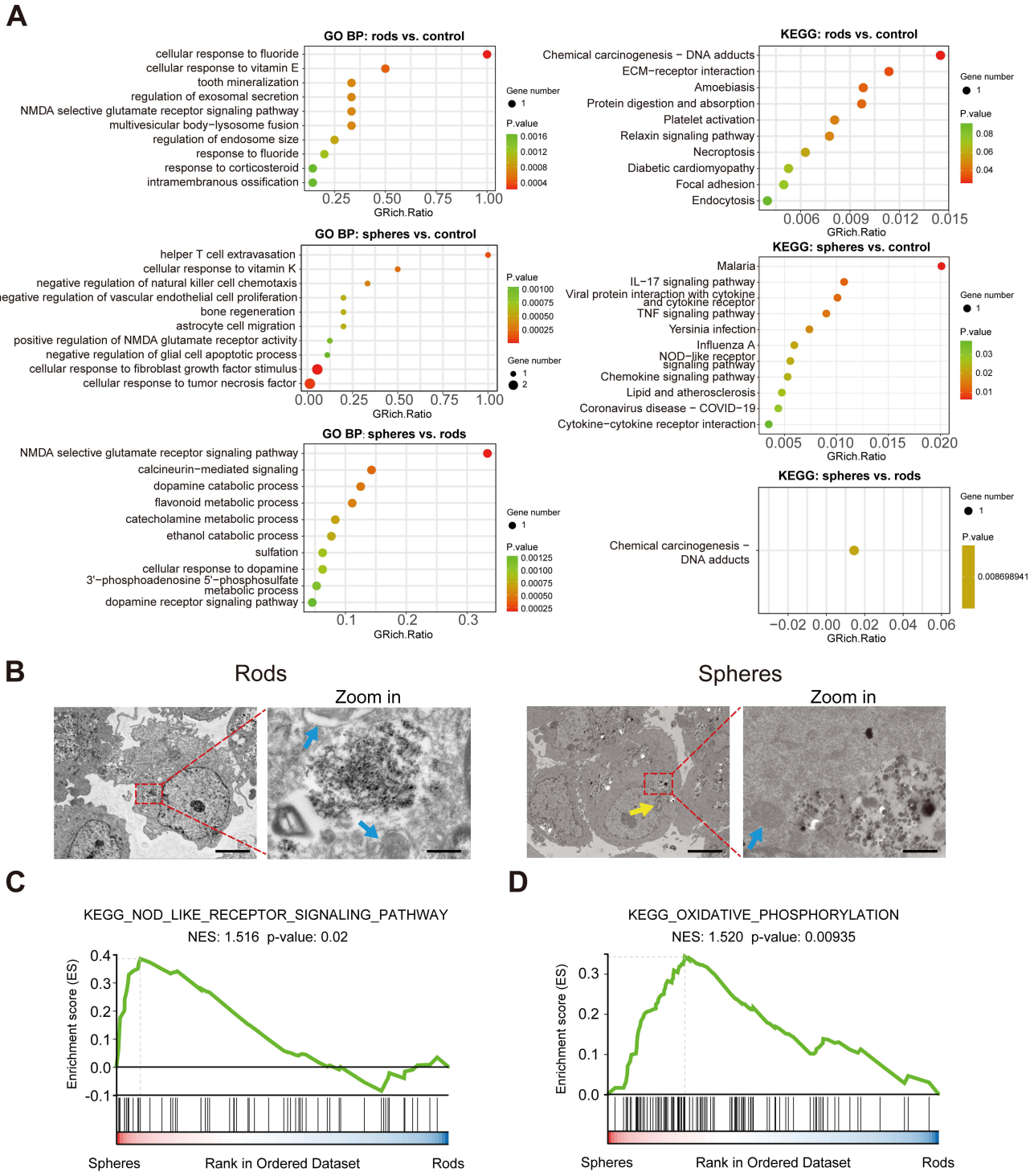

Figure 5 Enrichment analysis and validation of HUVEC monolayer following exposure to rods or spheres HAPNs. (**A**) Top 10 enriched GO biological process (BP) terms and KEGG pathway of DEGs after two groups comparison. (**B**) Representative TEM micrographs of HAPN treated HUVEC monolayer. Left panels are the whole-cell micrographs of rods and spheres HAPNs treated HUVEC monolayers, right panels are enlarged micrographs of red dotted line in left panels. Blue arrows indicate the mitochondria, yellow arrow indicates nuclear cleavage. Scale bars: left panels, 5 μm; right panels, 500 nm. (**C** and **D**) GSEA analysis of NOD-like receptor signaling pathway (**C**) and oxidative phosphorylation (**D**) in spheres HAPN-treated HUVEC monolayers compared with rods HAPN-treated HUVEC monolayers.

However, the IL-17, TNF, and NOD-like receptor signaling pathways were activated in HUVEC monolayers following treatment with spheres HANPs, as compared to the control group (Figure 5A and Figure S6). Among the signaling pathways activated in HUVECs post-exposure to spheres HANPs, IL-17, TNF, and NOD-like receptor

signaling pathways have been implicated in multiple studies as triggers of local host cell death.[47–49] The elevated expression of the pro-inflammatory molecule CCL2 in HUVECs following exposure to spheres HANPs at 200 μM contributed to the enrichment of biological processes and signaling pathways associated with pro-inflammatory responses. Uptake of spheres HANPs by HUVEC monolayers led to increased SULT1A3 expression, thereby promoting the chemical carcinogenesis-DNA adducts signaling pathway (Figure 5A and Figure S6), which indicates the release of chemically harmful substances into the nucleus, causing DNA damage. This finding aligns with the observed cell cycle distribution and DNA damage as depicted in Figure 2E and F. TEM images further validated the apoptotic/necrotic process and DNA damage induced by spheres HANPs, showing the disappearance and weakening of mitochondrial ridges and nucleus fragmentation (Figure 5B). Given the limitations of DEG enrichment analysis, some key genes with minor expression changes may be overlooked by the DEG criteria. GSEA analysis further demonstrated that exposure to spheres HANPs induced programmed cell apoptosis/necrosis in the inflammatory form of HUVEC monolayers, in contrast to exposure to rods HANPs (Figure 5C). These results indicate that spheres HANPs may induce apoptosis/necrosis and cell cycle arrest in HUVECs via inflammation-mediated pathways. Notably, treatment with spheres HANPs led to the enrichment of oxidative phosphorylation, further indicating that such treatment triggers cellular damage and necessitates the initiation of the oxidative phosphorylation biochemical process in HUVECs to mitigate damage (Figure 5D).[36,50] These results unequivocally demonstrate that the survival state of HUVEC monolayers, induced by HANPs exposure, is mediated through an endogenous pathway and correlates with the nanoparticles' surface area. The geometry of HANPs influences their endocytosis, intracellular distribution, and ultimately, the biological functions and pathways within the cells.

In vivo Cardiovascular Safety Assessment

To investigate the potential cardiovascular health hazards of HANPs after oral administration, freshly prepared rods or spheres HANPs in saline solution were administered via gavage to Balb/c mice at a dose of 500 μM/kg, with two administrations within 24 hours to emulate repeated administration. Electrocardiography (ECG), haematological assessments, and blood biochemical analyses were performed 1, 7, and 14 days after administration. The results showed that the administration of rods or spheres HANPs did not significantly interfere with cardiac pump function and circulation, as assessed by ECG (Figure 6A) and tabled data (Table S1). Furthermore, the body weights of the mice were not affected by the gavage administration of HANPs (Figure S7). In terms of the haematological assessments, standard markers pertaining to the leukocyte, erythrocyte, and platelet systems were evaluated. No meaningful differences were observed in the erythrocyte and platelet systems compared to the saline-treated mice, with the exception of the leukocyte system (Figure 6B and Figure S8). Serum biochemical analysis was performed to assess various parameters, including aspartate transaminase (AST), alanine transaminase (ALT), blood urea nitrogen (BUN), uric acid (UA), creatine kinase (CK), lactate dehydrogenase (LDH), total cholesterol (CHO), triglycerides (TG), blood glucose (GLU), and levels of Ca^{2+} and P^{5+} ions (Figure 6C and Figure S9). Dynamic changes in these parameters were noted during the testing period, indicating the entry of these nanoparticles into the circulation post-gavage. We found that higher serum levels of Ca^{2+} and P^{5+} in the mice treated with rods HANPs compared to those treated with spheres HANPs on the first day after gavage. As spheres HANPs accumulated in mouse VECs, leading to apoptosis/necrosis of these cells, the ruptured cell membranes of apoptotic/necrotic VECs permitted the re-entry of spheres HANPs and their dissolved products into the bloodstream. Consequently, mice treated with spheres HANPs exhibited higher serum levels of Ca^{2+} and P^{5+}, accompanied by an overall increase in biochemical parameters of major organs on days 7 and 14 after gavage.

In contrast, rods HANPs, which were not readily internalized by VECs and exhibited a relatively low number of surface Ca^{2+} cations, required more time to induce cell apoptosis/necrosis. As a result, the re-entry of rods HANPs and their dissolved products into the bloodstream was observed on the 14th day following gavage. This suggests that both rods and spheres HANPs that entered the bloodstream remained in the blood vessels for 14 days without being fully cleared. These results align with the bio-distribution findings of rods and spheres HANPs in the serum 14 days post-gavage (Figure S10). These data demonstrate that HANPs present in the bloodstream can directly impact the vascular endothelium and their effects are dependent on the geometry of the nanoparticles.

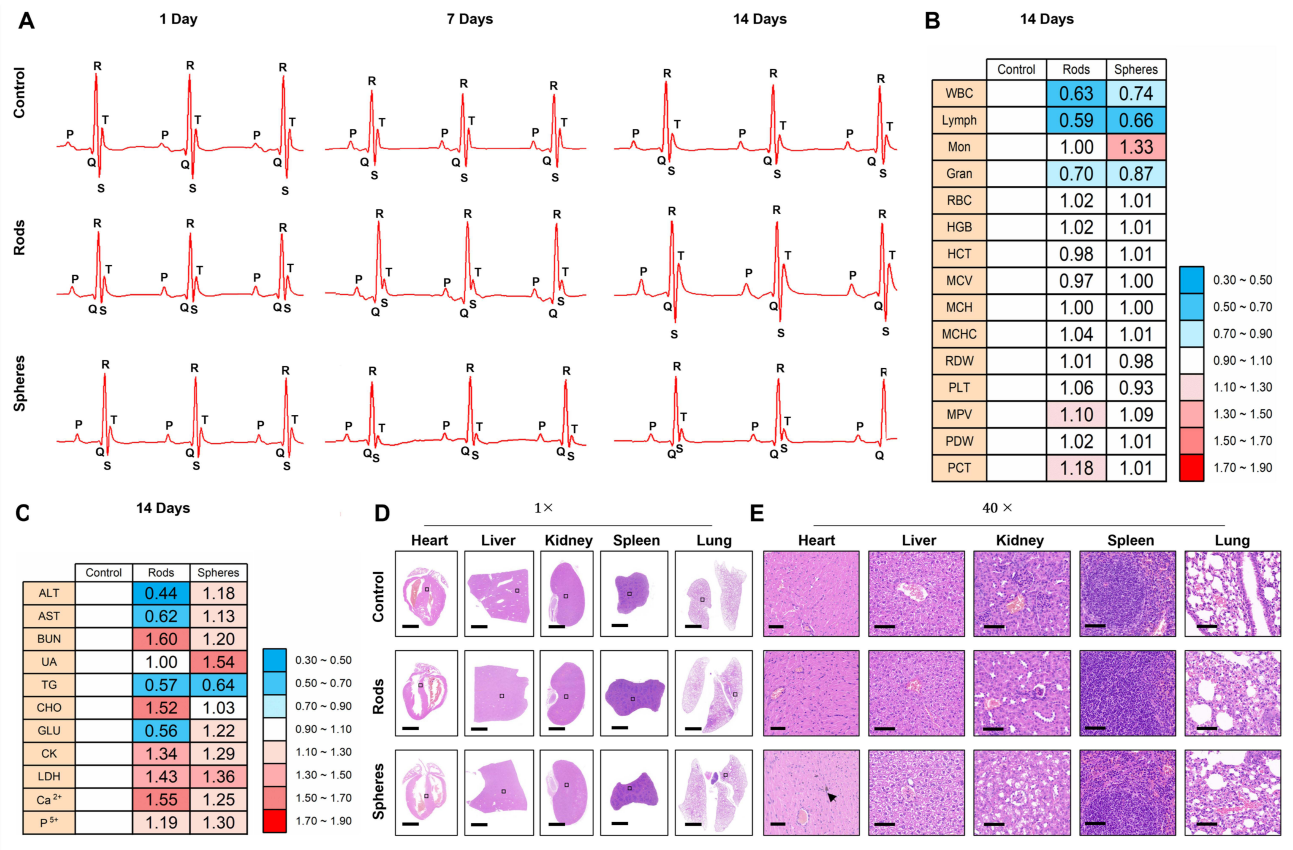

Figure 6 In vivo cardiovascular safety assessment after exposure to rods or spheres HAPNs. A, Representative ECGs of mice at 1, 7, and 14 days after gavage of saline, rods and spheres HAPNs. B, C, Heat map of representative haematological data (**B**) and serum biochemistry data (**C**) of mice with rods or spheres HAPNs at 14 days post-gavage. Data are displayed as relative quantification (RQ) to saline-treated mice. D, E, H&E staining of the heart, liver, kidney, spleen and lung at low magnification (**D**) and high magnification (**E**) of the saline, rods, or spheres HAPNs at 21 days post-gavage. Scar bars: (**D**),1000 μm; (**E**) 100 μm. The black box in (**D**) indicates the area of enlarged images in (**E**).

After 21 days of gavage, major organs, including the heart, liver, kidney, spleen, and lung, were collected from mice for histological analysis. At a low magnification of ×1, the organ structures in each group appeared intact (Figure 6D). At a higher magnification of ×40, there was no observable accumulation of rods or spheres HANPs in the examined organs. In mice treated with rods HANPs, a minor reversible kidney injury was observed. On the other hand, mice treated with spheres HANPs exhibited mild inflammation and slight reversible damage in the kidney, heart, liver, spleen, and lung (Figure 6E). This suggests that the circulation of spheres HANPs in the bloodstream induces a systemic inflammatory response, aligning with the changes observed in the white blood cell system in routine blood tests. Although in vivo experiments have shown that neither rods nor spheres HANPs exhibited significant side effects in mice when administered via gavage at a dose of 500 μM/kg, it is important to note that each mouse received only two gavage treatments, and the HANPs remained in the circulatory system for 14 days without being completely cleared.

Discussion

In vitro experiments allowed us to examine the impact of HANPs on HUVEC monolayers by analyzing the state and function of cells. In in vitro experiments, we used different concentrations of HANPs in the form of rods and spheres in culture with HUVEC, with the aim of observing the effect of the geometry of HANPs on the cellular state at different concentrations. Firstly, in the CCK-8 assay, HUVEC monolayers exhibited lower absorbance when exposed to sphere-shaped HANPs as opposed to rod-shaped HANPs (Figure 2A). This suggests that the geometry influences the viability of HUVEC monolayers following exposure to HANPs at 200 μM and 500 μM, with a higher surface area contributing to increased cytotoxicity. Furthermore, Figure 2B illustrates that HUVEC monolayers subjected to sphere-shaped HANPs exhibited an increased

number of dead cells. These results are consistent with a previous report indicating that higher surface area-to-mass ratios of nanoparticles are associated with greater cytotoxicity.[51] Similarly, in flow cytometry experiments, we determined that sphere-shaped HANPs exhibit an inhibitory effect on the proliferation of HUVECs. Given that the surface area of spheres HANPs is approximately 2.5 times larger than that of rods HANPs, the abundant Ca^{2+} cations on these nanoparticles' surface may directly cause apoptosis/necrosis and cell cycle arrest at the S-phase, thereby inhibiting the viability of the HUVEC monolayer.[37] After exposure to rod-shaped HANPs at 500 μM, the cell cycle of the HUVEC monolayer was arrested at the G0/G1 phase, indicating milder intracellular DNA damage and only a minor effect on cell cycle progression. DNA damage during this phase activates a transient DNA damage response, temporarily delaying the onset of the S-phase and providing additional time for DNA repair before replication.[52] Conversely, exposure to 500 μM sphere-shaped HANPs results in prolonged cell cycle arrest at the S-phase (Figure 2E and F), suggesting that higher concentrations of sphere-shaped HANPs sustain DNA damage. Since rods and spheres HANPs had no impact on the viability and cell cycle progression of HUVEC monolayers at 100 μM, this concentration was excluded from subsequent studies. These findings indicate that geometry influences the survival of HUVEC monolayers post-exposure to HANPs, with those possessing a higher surface area impairing viability more significantly.

We assessed HUVEC proliferation from another perspective through Ki67 fluorescence assays, and this result is in alignment with the findings from cell cycle experiments, which showed cell cycle arrest at the G0/G1 or S phases inhibits mitosis (Figure 3A and B). In eukaryotes, cell cycle arrest provides additional time for cells to repair DNA damage, thereby reducing mutation occurrence and preventing disease development.[53] In the wound-healing study, we discovered that higher doses of sphere-shaped HANPs adversely affect the "scratch" repair function of HUVEC monolayers (Figure 3E and F). Consistent with published reports, damage occurring during the S phase slows replication, while sustained DNA damage significantly reduces the DNA replication rate.[54] Jia et al evaluated the biocompatibility of three different shapes of nano hydroxyapatite (nanotubes, nanowires, and nanospheres) and found that these nano morphologies have different effects on osteoblasts. The results showed that compared to nanowires and nanotubes, spherical nano hydroxyapatite induced more ROS production in cells, which led to a decrease in cell activity, indicating that spherical nano hydroxyapatite has higher cytotoxicity.[55] Furthermore, Huang et al co cultured four different shapes of nano hydroxyapatite with aortic smooth muscle cells to investigate the effect of crystal shape on cell toxicity. Research has found that all shapes of nano hydroxyapatite have a negative effect on cell survival rate.[56] These findings indicate that exposure to HANPs may trigger a range of endogenous damage, correlating with particle geometry and surface area. Collectively, our data indicate that HANPs' geometry may influence nuclear mitosis in HUVECs through an intrinsic pathway. HANPs with larger surface areas hinder proliferation and delay repair DNA damage at higher concentrations.

In RNA transcriptome analysis, the expression of the HUVEC pro-inflammatory molecule CCL2 increased in the spherical HANPs group, contributing to the enrichment of biological processes and signaling pathways associated with pro-inflammatory responses. Meanwhile, through KEGG enrichment, IL-17, TNF, and NOD-like receptor signaling pathways were activated in the spherical HANPs group, which may be associated with the induction of cell death (Figure 5A and Figure S6). GSEA analysis further showed that exposure to spherical HANPs induced programmed apoptosis/necrosis in HUVEC monolayers through inflammatory processes, compared with exposure to rod HANPs. Thus, spherical HANPs may induce HUVEC apoptosis/necrosis and cell cycle arrest through inflammation-mediated pathways. The geometry of HANPs influences intracellular signaling communication and modifies the functional state of cells.

In vivo experiments, our findings suggest that rods and spheres HANPs do not systematically accumulate in major organs, indicating that the circulatory system is the primary target of HANPs. This result is consistent with previous epidemiological observations indicating that nanoparticles can enter the circulation.[27,51] Additionally, mouse vascular endothelial cells (VECs) demonstrate high sensitivity to the geometry of HANPs upon exposure. In contrast to rods HANPs, spheres HANPs, with their high specific surface area, can induce sustained endothelial injury in mice by triggering inflammation and apoptosis/necrosis of VECs. Endothelial injury constitutes a reversible alteration amenable to repair through methods such as exercise, calcium antagonists, angiotensin-converting enzyme inhibitors, and other therapeutic approaches. However, prolonged exposure to deleterious factors can precipitate cardiovascular events.[57] For example, activation of intracellular Ca^{2+} channels in VECs, vascular smooth muscle cells (VSMCs), and monocytes represents a critical mechanism in the formation of atherosclerotic plaques and vascular calcification.[58] In fact, the

capability of cardiovascular cells to differentiate into bone cells post-exposure to HANPs has been repeatedly confirmed.[59,60] Therefore, the apoptosis/necrosis and inflammation of VECs induced by spheres HANPs in the bloodstream may play a pivotal role in the development of chronic cardiovascular diseases, including atherosclerotic plaque and vascular calcification.[59,60] This finding correlates with the hypothesis that cardiovascular events stemming from nanoparticle exposure may be mediated by a systemic inflammatory response mechanism.[51] Chronic cardiovascular conditions, such as atherosclerotic plaque and vascular calcification, represent long-term processes that may intersect with factors like age, hypertension, hyperlipidemia, diabetes mellitus, and other diseases potentially related to inflammation. This conclusion necessitates further substantiation through additional animal studies.

Conclusion

In conclusion, this study determined that the geometry and surface area of HANPs significantly influence VEC survival status and proliferation. Spheres HANPs exhibited greater cytotoxicity because of their larger surface area, leading to inflammation mediated by CCL2 expression, endothelial cell apoptosis/necrosis and S-phase arrest, in comparison to rods HANPs (Figure 7). Importantly, our experimental system did not identify any significant systemic accumulation of HANPs in major organs. However, the repeated administration of HANPs-based agents possessing larger surface areas could result in persistent damage to the vascular endothelium. This highlights the critical role of nanoparticle geometry and surface area in vascular health and emphasizes the imperative for meticulous consideration in the design and utilization of nanomaterials in biomedical applications.

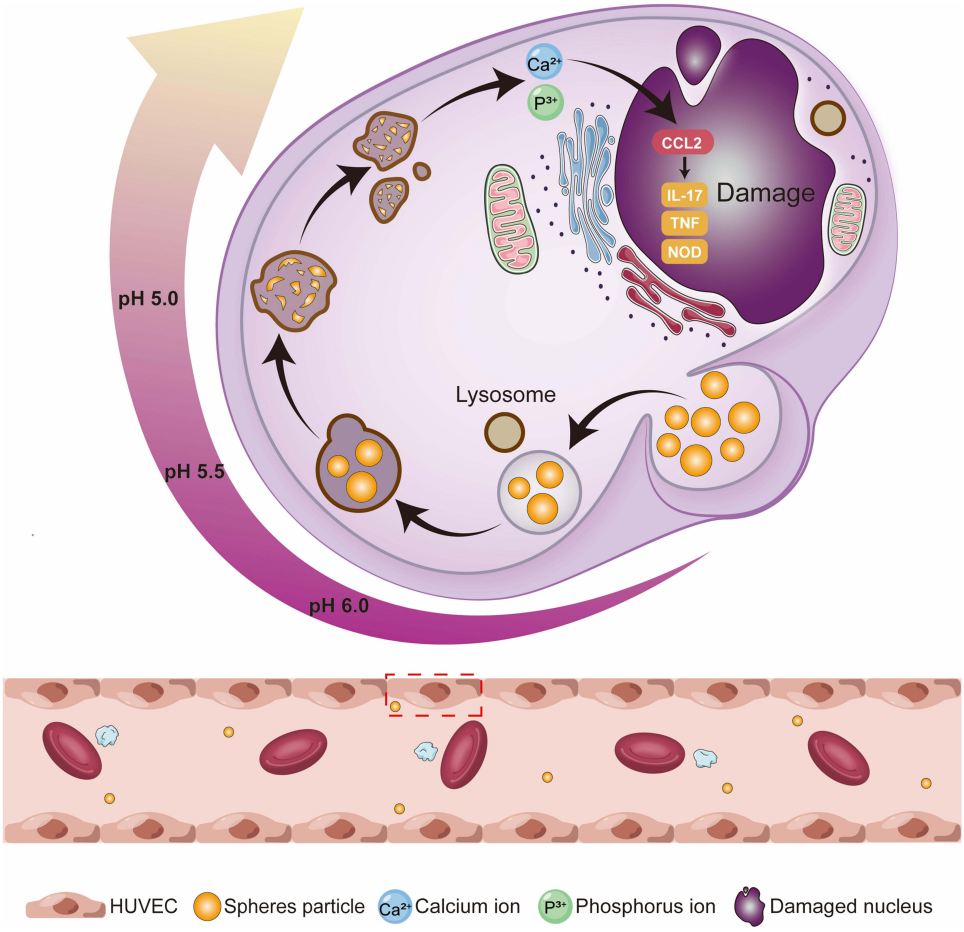

Figure 7 Sphere-shaped hydroxyapatite nanoparticles with a higher surface area induce inflammatory apoptosis/necrosis in vascular endothelial cells monolayer.

Acknowledgments

We are very grateful to Jiali Li for his contribution to this study, which has been of great help. In addition, this work was supported by the fund from the National Natural Science Foundation of China (No. 82070695 and No. 81900619), Guangdong Provincial Key Laboratory of Research in Structural Birth Defect Disease (No. B030301004), Guangzhou Science and Technology Project (No. A03J0444 and No. 202201020657), the Guangdong Natural Science Foundation (No. 2022A1515012610), and Guangdong Province Appropriate Technology in Health (No. 2023C-TS51) for financial support.

Disclosure

The authors report no conflicts of interest in this work.

References

1. Qi C, Musetti S, Fu LH, Zhu YJ, Huang L. Biomolecule-assisted green synthesis of nanostructured calcium phosphates and their biomedical applications. *Chem Soc Rev*. 2019;48(10):2698–2737. doi:10.1039/c8cs00489g
2. Ethirajan A, Ziener U, Chuvilin A, Kaiser U, Cölfen H, Landfester K. Biomimetic Hydroxyapatite Crystallization in Gelatin Nanoparticles Synthesized Using a Miniemulsion Process. *Adv Funct Mater*. 2008;18(15):2221–2227. doi:10.1002/adfm.200800048
3. Bera B, Saha Chowdhury S, Sonawane VR, De S. High capacity aluminium substituted hydroxyapatite incorporated granular wood charcoal (Al-HApC) for fluoride removal from aqueous medium: batch and column study. *Chem Eng J*. 2023;466. doi:10.1016/j.cej.2023.143264
4. Zhao H, Wu C, Gao D, et al. Antitumor Effect by Hydroxyapatite Nanospheres: activation of Mitochondria-Dependent Apoptosis and Negative Regulation of Phosphatidylinositol-3-Kinase/Protein Kinase B Pathway. *ACS nano*. 2018;12(8):7838–7854. doi:10.1021/acsnano.8b01996
5. Ding ZZ, Fan ZH, Huang XW, et al. Bioactive Natural Protein-Hydroxyapatite Nanocarriers for Optimizing Osteogenic Differentiation of Mesenchymal Stem Cells. *J Mat Chem B*. 2016;4(20):3555–3561. doi: 10.1039/c6tb00509h
6. Yang P, Quan Z, Li C, Kang X, Lian H, Lin J. Bioactive, luminescent and mesoporous europium-doped hydroxyapatite as a drug carrier. *Biomaterials*. 2008;29(32):4341–4347. doi:10.1016/j.biomaterials.2008.07.042
7. Ma X, Li Y, Wang C, et al. Controlled synthesis and transformation of nano-hydroxyapatite with tailored morphologies for biomedical applications. *J Mat Chem B*. 2017;5(46):9148–9156. doi: 10.1039/c7tb02487h
8. Chen Y, Yang L, Huang S, et al. Delivery system for DNAzymes using arginine-modified hydroxyapatite nanoparticles for therapeutic application in a nasopharyngeal carcinoma model. *Int j Nanomed*. 2013;8:3107–3118. doi:10.2147/ijn.S48321
9. Laranjeira MS, Moço A, Ferreira J, et al. Different hydroxyapatite magnetic nanoparticles for medical imaging: its effects on hemostatic, hemolytic activity and cellular cytotoxicity. *Colloids Surf B*. 2016;146. 363–374. doi:10.1016/j.colsurfb.2016.06.042
10. Chen X, Yang B, Qi C, et al. DNA-templated microwave-hydrothermal synthesis of nanostructured hydroxyapatite for storing and sustained release of an antibacterial protein. *Dalton Trans*. 2016;45(4):1648–1656. doi:10.1039/c5dt03357h
11. Geuli O, Metoki N, Eliaz N, Mandler D. Electrochemically Driven Hydroxyapatite Nanoparticles Coating of Medical Implants. *Adv Funct Mater*. 2016;26(44):8003–8010. doi:10.1002/adfm.201603575
12. Zheng X, Hui J, Li H, et al. Fabrication of novel biodegradable porous bone scaffolds based on amphiphilic hydroxyapatite nanorods. *Mater Sci Eng C Mater Biol Appl*. 2017;75. 699–705. doi:10.1016/j.msec.2017.02.103
13. Syamchand SS, Priya S, Sony G. Hydroxyapatite nanocrystals dually doped with fluorescent and paramagnetic labels for bimodal (luminomagnetic) cell imaging. *Mikrochim Acta*. 2014;182(5–6):1213–1221. doi:10.1007/s00604-014-1421-4
14. Sun TW, Yu WL, Zhu YJ, et al. Hydroxyapatite Nanowire@Magnesium Silicate Core-Shell Hierarchical Nanocomposite: synthesis and Application in Bone Regeneration. *ACS Appl Mater Interfaces*. 2017;9(19):16435–16447. doi:10.1021/acsami.7b03532
15. Wang X, Zhuang J, Peng Q, Li YD. Liquid–Solid–Solution Synthesis of Biomedical Hydroxyapatite Nanorods. *Adv Mater*. 2006;18 (15):2031–2034. doi:10.1002/adma.200600033
16. Shyong YJ, Wang MH, Tseng HC, Cheng C, Chang KC, Lin FH. Mesoporous Hydroxyapatite as Olanzapine Carrier Provides a Long-Acting Effect in Antidepression Treatment. *J Med Chem*. 2015;58(21):8463–8474. doi:10.1021/acs.jmedchem.5b00714
17. Sun Y, Chen Y, Ma X, et al. Mitochondria-Targeted Hydroxyapatite Nanoparticles for Selective Growth Inhibition of Lung Cancer in Vitro and in Vivo. *ACS App Mat*. 2016;8(39):25680–25690. doi:10.1021/acsami.6b06094
18. Shebi A, Lisa S. Pectin mediated synthesis of nano hydroxyapatite-decorated poly(lactic acid) honeycomb membranes for tissue engineering. *Carbohydr Polym*. 2018;201:39–47. doi:10.1016/j.carbpol.2018.08.012
19. Mi P, Kokuryo D, Cabral H, et al. A pH-activatable nanoparticle with signal-amplification capabilities for non-invasive imaging of tumour malignancy. *Nature Nanotechnol*. 2016;11(8):724–730. doi:10.1038/nnano.2016.72
20. Xu Z, Xia Y, Zhou P, et al. Silicon incorporation into hydroxyapatite nanocarrier counteracts the side effects of vancomycin for efficient chronic osteomyelitis treatment. *Chem Eng J*. 2021:406. 10.1016/j.cej.2020.126821.
21. Sarasati A, Wihadmadyatami H, Ana ID. Carbonate apatite nanoparticles: a novel nano-adjuvant for oral mucosal vaccines and immunomodulator. *OpenNano*. 2023;12:100149. doi:doi:10.1016/j.onano.2023.100149
22. Sari M, Ramadhanti DM, Amalina R, Yusuf Y, ANA ID, YUSUF Y. Development of a hydroxyapatite nanoparticle-based gel for enamel remineralization -A physicochemical properties and cell viability assay analysis. *Den Mater J*. 2022;41(1):68–77. doi:10.4012/dmj.2021-102
23. Anggraeni R, Ana ID, Wihadmadyatami H. Development of mucosal vaccine delivery: an overview on the mucosal vaccines and their adjuvants. *Clini Exper Vacc Res*. 2022;11(3):235–248. doi:10.7774/cevr.2022.11.3.235
24. Anggraeni R, Martien R, Agustina D, Ana ID. Incorporation of Ovalbumin into Carbonate Apatite as a Candidate for Protein Delivery. *Key Eng Mater*. 2018;782(782):27–31. doi:10.4028/www.scientific.net/KEM.782.27
25. Anggraeni R, Ana ID, Agustina D, Martien R. Induction of protein specific antibody by carbonated hydroxy apatite as a candidate for mucosal vaccine adjuvant. *Den Mater J*. 2022;41(5):710–723. doi:10.4012/dmj.2021-254

26. Zhang Y, Zhu J, Li S, et al. Rational design of highly H2O- and CO2-tolerant hydroxyapatite-supported Pd catalyst for low-temperature methane combustion. *Chem Eng J*. 2020:396. 10.1016/j.cej.2020.125225.
27. Donaldson K, Duffin R, Langrish JP, et al. Nanoparticles and the cardiovascular system: a critical review. *Nanomedicine*. 2013;8(3):403–423. doi:10.2217/nnm.13.16
28. Yu X, Hong F, Zhang YQ. Bio-effect of nanoparticles in the cardiovascular system. *J Biomed Mater Res Part A*. 2016;104(11):2881–2897. doi:10.1002/jbm.a.35804
29. Zhang L, Feng G, Yang S, et al. Polyethylenimine-Modified Mesoporous Silica Nanoparticles Induce a Survival Mechanism in Vascular Endothelial Cells via Microvesicle-Mediated Autophagosome Release. *ACS nano*. 2021;15(6):10640–10658. doi:10.1021/acsnano.1c03456
30. Hou CH, Hou SM, Hsueh YS, Lin J, Wu HC, Lin FH. The in vivo performance of biomagnetic hydroxyapatite nanoparticles in cancer hyperthermia therapy. *Biomaterials*. 2009;30(23–24):3956–3960. doi:10.1016/j.biomaterials.2009.04.020
31. Zhao B, Zeng L, Chen D, et al. NIR-photocatalytic regulation of arthritic synovial microenvironment. *Sci Adv*. 2022;8(40):eabq0959. doi:10.1126/sciadv.abq0959
32. Wei H, Jiang D, Yu B, et al. Nanostructured polyvinylpyrrolidone-curcumin conjugates allowed for kidney-targeted treatment of cisplatin induced acute kidney injury. *Bioact Mater*. 2023;19:282–291. doi:10.1016/j.bioactmat.2022.04.006
33. Shi X, Zhou K, Huang F, Wang C. Interaction of hydroxyapatite nanoparticles with endothelial cells: internalization and inhibition of angiogenesis in vitro through the PI3K/Akt pathway. *Int j Nanomed*. 2017;12:5781–5795. doi:10.2147/ijn.S140179
34. Pezzatini S, Solito R, Morbidelli L, et al. The effect of hydroxyapatite nanocrystals on microvascular endothelial cell viability and functions. *J Biomed Mater Res Part A*. 2006;76(3):656–663. doi:10.1002/jbm.a.30524
35. Santos C, Turiel S, Sousa Gomes P, et al. Vascular biosafety of commercial hydroxyapatite particles: discrepancy between blood compatibility assays and endothelial cell behavior. *J Nanobiotechnol*. 2018;16(1):27. doi:10.1186/s12951-018-0357-y
36. Hinde E, Thammasiraphop K, Duong HT, et al. Pair correlation microscopy reveals the role of nanoparticle shape in intracellular transport and site of drug release. *Nature Nanotechnol*. 2017;12(1):81–89. doi:10.1038/nnano.2016.160
37. Ewence AE, Bootman M, Roderick HL, et al. Calcium phosphate crystals induce cell death in human vascular smooth muscle cells: a potential mechanism in atherosclerotic plaque destabilization. *Circulation Res*. 2008;103(5):e28–34. doi:10.1161/circresaha.108.181305
38. Nadra I, Mason JC, Philippidis P, et al. Proinflammatory activation of macrophages by basic calcium phosphate crystals via protein kinase C and MAP kinase pathways: a vicious cycle of inflammation and arterial calcification? *Circulation Res*. 2005;96(12):1248–1256. doi: 10.1161/01.RES.0000171451.88616.c2
39. Nadra I, Boccaccini AR, Philippidis P, et al. Effect of particle size on hydroxyapatite crystal-induced tumor necrosis factor alpha secretion by macrophages. *Atherosclerosis*. 2008;196(1):98–105. doi:10.1016/j.atherosclerosis.2007.02.005
40. Tang L, Tang Y, Zhang J, et al. High-strength super-hydrophobic double-layered PBO nanofiber-polytetrafluoroethylene nanocomposite paper for high-performance wave-transparent applications. *Sci Bull*. 2022;67(21):2196–2207. doi:10.1016/j.scib.2022.10.011
41. Ma Z, Kang S, Ma J, et al. Ultraflexible and Mechanically Strong Double-Layered Aramid Nanofiber-Ti(3)C(2)T(x) MXene/Silver Nanowire Nanocomposite Papers for High-Performance Electromagnetic Interference Shielding. *ACS nano*. 2020;14(7):8368–8382. doi:10.1021/acsnano.0c02401
42. Zhang W, Zhang YS, Bakht SM, et al. Elastomeric free-form blood vessels for interconnecting organs on chip systems. *Lab on a Chip*. 2016;16(9):1579–1586. doi:10.1039/c6lc00001k
43. Cheng F, Cao X, Li H, et al. Generation of Cost-Effective Paper-Based Tissue Models through Matrix-Assisted Sacrificial 3D Printing. *Nano Lett*. 2019;19(6):3603–3611. doi:10.1021/acs.nanolett.9b00583.
44. Niu Y, Zhang B, Galluzzi M. An amphiphilic aggregate-induced emission polyurethane probe for in situ actin observation in living cells. *J Colloid Interface Sci*. 2021;582(Pt B):1191–1202. doi:10.1016/j.jcis.2020.08.113
45. Niu Y, Galluzzi M, Fu M, Hu J, Xia H. In vivo performance of electrospun tubular hyaluronic acid/collagen nanofibrous scaffolds for vascular reconstruction in the rabbit model. *J Nanobiotechnol*. 2021; 19(1):349. doi:10.1186/s12951-021-01091-0
46. Niu Y, Galluzzi M, Deng F, et al. A biomimetic hyaluronic acid-silk fibroin nanofiber scaffold promoting regeneration of transected urothelium. *Bioeng Transl Med*. 2022;7(2):e10268. doi:10.1002/btm2.10268
47. Gaffen SL. Structure and signalling in the IL-17 receptor family. *Nat Rev Immunol*. 2009;9(8):556–567. doi:10.1038/nri2586
48. Lemos DR, Babaeijandaghi F, Low M, et al. Nilotinib reduces muscle fibrosis in chronic muscle injury by promoting TNF-mediated apoptosis of fibro/adipogenic progenitors. *Nature Med*. 2015;21(7):786–794. doi:10.1038/nm.3869
49. Saur IML, Panstruga R, Schulze-Lefert P. NOD-like receptor-mediated plant immunity: from structure to cell death. *Nat Rev Immunol*. 2021;21(5):305–318. doi:10.1038/s41577-020-00473-z
50. Huang T, Zhang T, Jiang X, et al. Iron oxide nanoparticles augment the intercellular mitochondrial transfer-mediated therapy. *Sci Adv*. 2021;7(40):eabj0534. doi:10.1126/sciadv.abj0534
51. Brook RD, Franklin B, Cascio W, et al. Air pollution and cardiovascular disease: a statement for healthcare professionals from the Expert Panel on Population and Prevention Science of the American Heart Association. *Circulation*. 2004;109(21):2655–2671. 10.1161/01.Cir.0000128587.30041.C8.
52. Murray JM, Carr AM. Integrating DNA damage repair with the cell cycle. *Curr Opin Cell Biol*. 2018;52:120–125. doi:10.1016/j.ceb.2018.03.006
53. Haber JE. A Life Investigating Pathways That Repair Broken Chromosomes. *Annual review of genetics*. *Annual Review of Genetics*. 2016; 50;1–28. doi:10.1146/annurev-genet-120215-035043
54. Paulovich AG, Hartwell LH. A checkpoint regulates the rate of progression through S phase in S. cerevisiae in response to DNA damage. *Cell*. 1995;82(5):841–847. doi:10.1016/0092-8674(95)90481-6
55. Jia Y, Qin L, Gong Y, et al. Experimental and theoretical investigations of the influences of one-dimensional hydroxyapatite nanostructures on cytocompatibility. *J Biomed Mater Res Part A*. 2021;109(5):804–813. doi:10.1002/jbm.a.37068
56. Huang LH, Sun XY, Ouyang JM. Shape-dependent toxicity and mineralization of hydroxyapatite nanoparticles in A7R5 aortic smooth muscle cells. *Sci Rep*. 2019;9(1):18979. doi:10.1038/s41598-019-55428-9
57. Demer LL, Tintut Y. Vascular calcification: pathobiology of a multifaceted disease. *Circulation*. 2008;117(22):2938–2948. doi:10.1161/circulationaha.107.743161

58. Demer L, Tintut Y. The roles of lipid oxidation products and receptor activator of nuclear factor-κB signaling in atherosclerotic calcification. *Circulation Res*. 2011;108(12):1482–1493. doi:10.1161/circresaha.110.234245
59. Proudfoot D, Davies JD, Skepper JN, Weissberg PL, Shanahan CM. Acetylated low-density lipoprotein stimulates human vascular smooth muscle cell calcification by promoting osteoblastic differentiation and inhibiting phagocytosis. *Circulation*. 2002;106(24):3044–3050. doi:10.1161/01.cir.0000041429.83465.41
60. Bobryshev YV, Killingsworth MC, Lord RS, Grabs AJ. Matrix vesicles in the fibrous cap of atherosclerotic plaque: possible contribution to plaque rupture. *J Cell & Mol Med*. 2008;12(5b):2073–2082. doi:10.1111/j.1582-4934.2008.00230.x

International Journal of Nanomedicine Dovepress

Publish your work in this journal

The International Journal of Nanomedicine is an international, peer-reviewed journal focusing on the application of nanotechnology in diagnostics, therapeutics, and drug delivery systems throughout the biomedical field. This journal is indexed on PubMed Central, MedLine, CAS, SciSearch®, Current Contents®/Clinical Medicine, Journal Citation Reports/Science Edition, EMBase, Scopus and the Elsevier Bibliographic databases. The manuscript management system is completely online and includes a very quick and fair peer-review system, which is all easy to use. Visit http://www.dovepress.com/testimonials.php to read real quotes from published authors.

Submit your manuscript here: https://www.dovepress.com/international-journal-of-nanomedicine-journal